

Physics-inspired adaptations to low-parameter neural network weather forecasts systems

Sebastian Scher^{a,b}, Gabriele Messori^{b,c}

^a *Know-Center Research GmbH, Graz, Austria*

^b *Department of Meteorology and Bolin Centre for Climate Research, Stockholm University, Stockholm, Sweden*

^c *Department of Earth Sciences and Centre of Natural Hazards and Disaster Science, Uppsala University, Uppsala, Sweden*

Corresponding author: Sebastian Scher, sscher@know-center.at

ABSTRACT: Recently, there has been a surge of research on data-driven weather forecasting systems, especially applications based on convolutional neural networks (CNNs). These are usually trained on atmospheric data represented on regular latitude-longitude grids, neglecting the curvature of the Earth. We assess the benefit of replacing the standard convolution operations with an adapted convolution operation which takes into account the geometry of the underlying data (Spherenet convolution), specifically near the poles. Additionally, we assess the effect of including the information that the two hemispheres of the Earth have “flipped” properties - for example cyclones circulating in opposite directions - into the structure of the network. Both approaches are examples of physics-informed machine learning. The methods are tested on the WeatherBench dataset, at a resolution of $\sim 1.4^\circ$ which is higher than many previous studies on CNNs for weather forecasting. For most lead times up to day +10 for 500 hPa geopotential and 850 hPa temperature, we find that using Spherenet convolution or including hemisphere-specific information individually lead to improvement in forecast skill. Combining the two methods typically gives the highest forecast skill. Our version of Spherenet is implemented flexibly and scales well to high resolution datasets, but is still significantly more expensive than a standard convolution operation. Finally, we analyze cases with high forecast error. These occur mainly in winter, and are relatively consistent across different training realizations of the networks, pointing to flow-dependent atmospheric predictability.

1. Introduction

Weather forecasting has for decades been dominated by numerical models built on physical principles, the so-called Numerical Weather Prediction Models (NWP). These models have seen a constant increase in skill over time (Bauer et al. 2015). Recently, however, there has been a surge of interest in data-driven weather forecasting in the medium-range (~ 2 -14 days ahead). These have often - but not exclusively, used neural networks (e.g. Scher (2018); Scher and Messori (2019b); Dueben and Bauer (2018); Weyn et al. (2019, 2020); Faranda et al. (2021); Scher and Messori (2020); Rasp and Thuerey (2021); Bi et al. (2022); Keisler (2022); Pathak et al. (2022); Chen et al. (2023); Lam et al. (2023); Ben-Bouallegue et al. (2023)), also in combination with physics-based models (e.g. Arcomano et al. (2022)). A historic overview of paradigms in weather prediction, is outlined in Balaji (2020). The use of convolutional neural networks (CNNs) (e.g. Scher (2018); Scher and Messori (2019b); Weyn et al. (2019); Rasp and Thuerey (2021)) or of a local network that is shared across the domain (Dueben and Bauer 2018), dominated in the early data-driven approaches. What these methods have in common is that they use global data on a regular lat-lon grid. This leads to distortions, especially close to the poles (Coors et al. 2018). However, a standard convolution or shared local architecture does not take such distortion into account since it uses a filter whose size is a fixed number of gridpoints (e.g. 3×3). Therefore, the area that the filter sees is not the same close to the Equator and close to the poles. Weyn et al. (2020) have proposed a solution to this problem via working on a different grid. Specifically, they regrid the data to a “cubed sphere” consisting of 6 different regions. Then, they use a standard convolution operation on each side of the cubed sphere. Additionally, they do not share the weights of the filters globally (as in the original architecture proposed by Scher (2018) and adapted to real world data by Weyn et al. (2019)), but instead use an independent convolution operation for the different sides of the cubed sphere. The weights are shared only for the two polar parts of the cubed sphere, but then “flipped” from one pole to the other to account for the different direction of rotation.

There are also other possibilities for including the spherical nature of the Earth in NN-based weather prediction models. Most of the currently best-performing models use either transformer-based methods (Bi et al. 2022) or graph neural networks (GNNs) (Keisler 2022; Lam et al. 2023). The approaches with GNNs consider the spherical nature of the earth via mapping into an abstract feature space on an icosahedral grid (Keisler 2022), or on grids on a multi-mesh representation

(Lam et al. 2023). The transformer architecture of Bi et al. (2022) uses a "3D Earth-specific transformer". In practice, the spherical nature is dealt with an Earth-specific positional bias in the transformer.

A drop-in replacement for convolution layers is presented in Esteves et al. (2023). They use a highly optimized form of spherical convolution based on spherical harmonics, and showed it can successfully be integrated into ML models for weather forecasting, having a skill comparable to state-of-the-art architectures.

In this paper, we present an alternative approach to incorporate the spherical nature of the Earth into CNNs. We use the SphereNet architecture, which has previously been proposed for classification tasks on 360°-images (Coors et al. 2018). Additionally, we test two different approaches for including information on the characteristics of the two hemispheres into our networks. All these approaches can be seen as variants of "informed machine learning" (von Rueden et al. 2020; Kashinath et al. 2021), in which prior knowledge is included into the machine-learning pipeline. In our case, the prior knowledge is that the Earth is spherical (in contrast to the regular data that we provide), and that the dynamics of the two hemispheres are – to some extent – "flipped" relative to each other. This information is directly encoded into the structure of the neural network.

Many of the latest transformer and GNN-based weather predictions models come with high technical and computational demands. While these architectures can outperform CNNs, we see a benefit in testing the limits of CNNs with a limited number of parameters, especially for research groups who may not have enough computational capacity to run very large transformer or GNN models. Therefore, the aim of this paper is not to create the best data-driven weather forecasts (and indeed we note that there are published architectures that perform more skillful predictions). Instead, we present two possible improvements to older CNN-based models, and disentangle their individual contributions to forecast skill. The improvements presented here are conceptually simple, and stem from physical reasoning. We believe that the experiments presented here will support future development of physics-oriented ML weather prediction models, despite the fact that large GNN and transformer based models currently have superior skill. We use a testbed reanalysis data from the WeatherBench dataset (Rasp et al. 2020), at a resolution of up to 1.4°. This is higher than many previous studies which used CNNs. Finally, we include an analysis of the events with highest forecast errors. These are important from an end-user point of view, and

TABLE 1. Overview of input data variables and spatial and temporal resolutions

input variable	spatial resolution lres / hres	temporal resolution
temperature 850hPa	2.8125° / 1.40625°	6h
temperature 500hPa	2.8125° / 1.40625°	6h
geopotential 850hPa	2.8125° / 1.40625°	6h
geopotential 500hPa	2.8125° / 1.40625°	6h
top-of-atmosphere incident radiation	2.8125° / 1.40625°	6h
orography	2.8125° / 1.40625°	time-invariant
land-sea mask	2.8125° / 1.40625°	time-invariant

in NWP models they have elicited significant attention. The occurrence of unusually bad forecasts (“forecast busts”) in NWP models is connected with specific weather situations (Rodwell et al. 2013; Lillo and Parsons 2017), and more generally, different weather situations have different predictability (Ferranti et al. 2015; Matsueda and Palmer 2018). We analyze whether the poorest forecasts of our data-driven forecasts systems are, as in NWP, associated with specific weather situations.

2. Methods

a. Data

We use data from WeatherBench (Rasp et al. 2020). This is a dataset specifically designed for benchmarking machine-learning based weather forecasts. The subset we use consists of ERA5 reanalysis data, regridded to a regular lat-lon grid with two different resolutions: 2.8125° (hereafter called “low-resolution” or “lres”) and 1.40625° (hereafter called “high-resolution” or “hres”). The following input variables are used: temperature at 850 hPa, geopotential at 300, 500, 700 and 1000 hPa, as well as top-of-the-atmosphere incident solar radiation. As evaluation variables, we use geopotential at 500hPa (“z500”) and temperature at 850hPa (“t850”). As additional time-invariant input variables, the land-sea mask and orography from ERA5 are used. We use the period 1979–2016 for training and validation, and 2017–2018 for evaluation (as proposed in WeatherBench). Following WeatherBench, all results presented in this paper are on the independent evaluation data that is not used for training and validation. The temporal resolution of the data is 6 hours. An overview of the input data is given in table 1.

b. Spherenet Convolution

In normal convolution, for each gridpoint, a fixed number of gridpoints in the vicinity are sampled (for example a 3×3 box centered on the gridpoint). For data on a globe (such as global atmospheric data) represented on a regular grid, this leads to distortions except very close to the equator. Indeed, a fixed neighborhood defined via the number of gridpoints corresponds to rectangles of differing size, depending on latitude. One way to remedy this is through the use of adapted convolution filters. Coors et al. (2018) proposed the SphereNet architecture in neural networks for image detection in spherical images.

With this method, instead of a box of fixed size in gridpoint space, each gridpoint is assigned a rectangle with fixed size in real space. Since the positions of available gridpoints and the target coordinates in this fixed-size box do not necessarily coincide, the target can also be an interpolation of up to four gridpoints. The principle is sketched in Fig. 1 a).

In normal convolution operations in neural networks, the kernel is always made up of exact gridpoints (e.g. a 3×3 box corresponding to 9 gridpoints). Our approach requires interpolation, and thus our method also allows the use of a non-integer number of gridpoints in the kernel. For example, we could use the distances $-1, -0.5, 0, 0.5, 1$ along the longitude direction, creating a kernel of 5 gridpoints. These 5 points then cover, with equal spacing, the distance that is normally covered by three kernel points (this distance that is is, in km, the distance of three gridpoints at the equator).

An alternative method for adapting convolution operators to the Earth's approximately spherical geometry that would seem promising in our case was proposed by Boomsma and Frellsen (2017), who presented convolution on a cubed sphere, where the sphere is divided into 6 parts. This is the same approach as in Weyn et al. (2020), but with weight-sharing across all 6 parts. The main limitation of this approach is that translational invariance of the convolution filters is lost. Specifically, in our application, the filters would not necessarily be aligned along the longitude and latitude circles. This is a potential problem, as there is physical meaning to these (a gradient in a certain variable along the latitude dimension is physically not the same as along the longitude dimension).

Cohen et al. (2018) compute spherical convolution via FFTs, resulting in full rotational invariance. As noted by Coors et al. (2018) this is not always a desired property, as it assumes that all directions

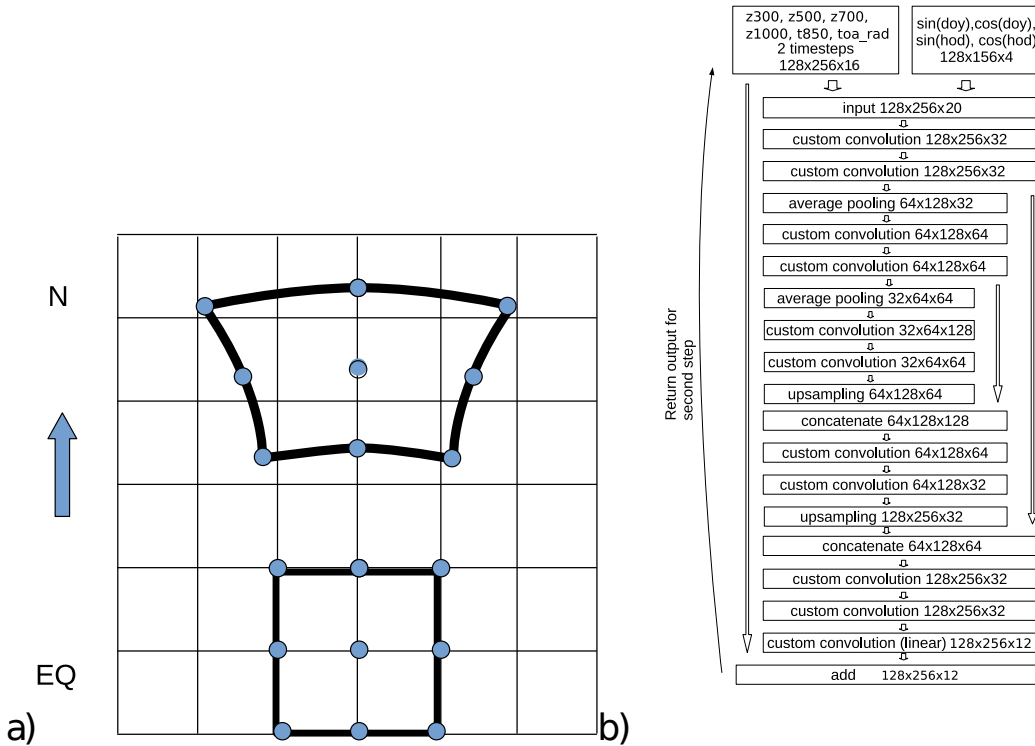


FIG. 1. a) Sketch of the principle of Spherenet convolution. Shown is a 3×3 kernel (corresponding to 3×3 gridpoints at the equator). b) Overview of our neural network structure. Dimensions are for the high-resolution data.

(e.g. in our case along longitude, along latitude or any other direction) are equivariant. As we discussed above, in our setting this is not physically meaningful. Eder et al. (2019) presents an approach that generalizes the method from Coors et al. (2018) to any type of structured data. Jiang et al. (2019) present an approach that works for unstructured grids.

Due to the limitations of the methods from Boomsma and Frellsen (2017) and Cohen et al. (2018) discussed above, and the fact that for our setting we don't need the generalized approaches from Eder et al. (2019), and Jiang et al. (2019), we opted for using the approach from Coors et al. (2018). We will refer to this approach as Spherenet convolution.

1) IMPLEMENTATION

Since Coors et al. (2018) have not provided details on their technical implementation, and since their code is not publicly available, we have designed our own implementation of Spherenet. In this section we use the word "tensor" as it is used in computational packages such as tensorflow, thus

interchangeably with “array”. Therefore, not everything referred to as a tensor here is necessarily a tensor in the strict mathematical sense of the term.

We have implemented Spherenet with the following steps (the channel dimension of the neural network is omitted here for simplification):

1. we start with a (fixed) filter kernel \vec{K} of length n , consisting of n pairs of lat-lon distances $\Delta p_i = (\Delta y_i, \Delta x_i)$, corresponding to gridpoints at the equator. A 3×3 kernel without fractional distances for example would be $[(-1, -1), (-1, 0), (-1, 1), (0, -1), (0, 0), (0, 1), (1, -1), (1, 0), (1, 1)]$.
2. for each of the $N \times M$ input gridpoints $p = (x, y)$ in the regular grid, we compute n pairs of (potentially non-integer) coordinates $p' = (y'_i, x'_i)$, corresponding to the n points in the kernel \vec{K} , transformed for the current position of p on the globe with the following equations. x and y are in gridpoint coordinates, and ϕ and θ are in radians.

$$\phi' = \arcsin v \sin \phi + \frac{\Delta \phi \sin v \cos \phi}{\rho} \quad (1)$$

$$\theta' = \theta + \arctan \left(\frac{\Delta x \sin v}{\rho} \cos \phi \cos v - \Delta y \sin \phi \sin v \right) \quad (2)$$

$$\rho = \sqrt{(\Delta \rho)^2 + (\Delta \theta)^2} \quad (3)$$

$$v = \arctan \rho \quad (4)$$

$$\Delta \phi = \Delta y \frac{\pi}{N} \quad (5)$$

$$\Delta \theta = \Delta x \frac{2\pi}{M} \quad (6)$$

$$y' = \phi' \frac{M}{\pi} + \frac{N-1}{2} \quad (7)$$

$$x' = \theta' \frac{M}{2\pi} \quad (8)$$

with latitude ϕ of the central point. The transformed coordinates ϕ' and θ' are in regular lat-lon coordinates, and x' and y' the corresponding coordinate indices on the regular lat-lon grid. The transformed coordinate indices for each gridpoint and kernel points are combined in a coordinate tensor \hat{A} of shape $N \times M \times n$.

3. the input \vec{x} data is flattened to \vec{x}_{flat} with shape $L = N \cdot M$, and the coordinate tensor \hat{A} is flattened to a tensor of shape $L \times n$, with the coordinates transformed to flattened coordinates.
4. a sparse interpolation tensor \hat{L} of size $L \times L$ is created, and filled with the target coordinates in such a way that multiplying the flattened input data \vec{x}_{flat} with the interpolation tensor results in the expanded input data $\vec{x}_{exp} = \hat{L}\vec{x}$ with shape $L \times n$. \hat{L} is implemented as a sparse tensorflow tensor. This implementation allows the use also on very large grids (large L), as only the non-zero components are kept in memory.
5. on \vec{x}_{exp} , a standard 1-d convolution with kernel size n (as implemented in major neural network libraries such as tensorflow) can now be applied, resulting in \vec{x}_{out} with size L , which is then unflattened to shape $N \times M$

The steps 1 and 2, and the computation of the interpolation tensor, need to be performed only once (when setting up the network). \hat{L} is stored in memory for all subsequent operations.

At gridpoints close to the poles, kernel-points can “pass” through the pole. For these points, not only the longitude, but also the latitude is adjusted. For example, on a $1 \times 1^\circ$ grid, a kernel point that without this adjustment would correspond to the impossible point $90.5^\circ\text{N } 0^\circ\text{E}$ will be set as $89.5^\circ\text{N } 180^\circ\text{E}$. With this, the “polar problem” of regular grids is eliminated.

c. Neural network architecture

We use a neural network architecture based on that proposed in Weyn et al. (2020), namely a U-net architecture. Weyn et al. (2020) however do not use data on a regular grid, but on a cubed sphere, consisting of several regular grids. They further use two sets of weights, across six different regions. We use the same architecture, but with each of their special convolution layers replaced by a standard convolution, Spherenet convolution and/or hemisphere-wise convolution (see below). The network structure is shown in Fig. 1 b). Our networks are implemented in tensorflow (Martín

Abadi et al. 2015) using the dataset api with tensorflow record files, resulting in an implementation that should also scale to datasets with higher resolution than the ones used here.

In addition to the input variables from ERA5 discussed in Sect. 2.a, day of the year (“doy”) and local hour of the day (“hod”, different for each longitude band) are used as additional input variables. Since these are “circular” variables, each of them is converted to two variables. Using two variables should make it easier for the model to learn the circular relationship (e.g. that doy 1 and doy 365 are adjacent days):

$$doy1 = \sin\left(\frac{2\pi}{365}doy\right) \quad (9)$$

$$doy2 = \cos\left(\frac{2\pi}{365}doy\right) \quad (10)$$

$$hod1 = \sin\left(\frac{2\pi}{24}hod\right) \quad (11)$$

$$hod2 = \cos\left(\frac{2\pi}{24}hod\right) \quad (12)$$

These 4 scalars are extended to the grid-resolution of the data and added as additional channels. The input of the networks is comprised of two timesteps of the 6 ERA5 inputs (resulting in 12 input channels), but the additional 4 variables (doy1, doy2, hod1, hod2) are provided only once, resulting in 12+4=16 input channels. The outputs of the networks are 2 timesteps of the input variables, without the additional variables (thus 12 channels). One forecast step is made of two consecutive passes through the network, via feeding the output back to the input, resulting in a 24 hour forecast. For details, see Weyn et al. (2020).

For consecutive forecasts (longer than 24 hours), hod is not updated, since each forecast step is 24 hours. We also choose not to update doym, since the forecast length of 10 days is very short compared to seasonal variations.

1) BASE ARCHITECTURE

Our base architecture without Spherenet convolution uses normal convolution with wrapping on the sides. Along the longitude direction the convolution is “wrapped” around, so there is no artificial boundary. At the poles the grid is wrapped over the pole: the northern neighbour of

a point on the northernmost latitude band is the point on the same latitude band but with 180° shifted longitude. The kernel size of the convolutions is 3×3 . Note that for the different resolution datasets, this corresponds to different spatial extents in the input data.

2) SPHERENET CONVOLUTION ARCHITECTURE

The Spherenet convolution architecture is the same as the base architecture, except that each convolution operation is replaced by a Spherenet convolution operation. Since the convolution deals both with the poles and the longitude-wrap, no padding is applied. We use a 3×3 kernel, just as in the base architecture.

3) HEMISPHERIC CONVOLUTION

We use two related approaches for incorporating the fact there are 2 hemispheres into the networks. In the first, we use separate (independent) convolution operations (with separate weights) for each hemisphere. The data is split at the equator. For the architecture without Spherenet convolution, the first row of the other hemisphere is added as padding for the boundary of the convolution, and the padding at the pole is handled in the same way as in the base architecture. When using Spherenet convolution together with hemispheric convolution this is not necessary, as this is included in the interpolation for the Spherenet convolution. Then, on each hemisphere, a convolution operation is performed. These will be referred to as “hemconv” and “sphereconv_hemconv”, respectively. In the second approach, the same convolution operation is used for both hemispheres, with the filter “flipped” along the lat dimension for the second hemisphere. This will be referred to as “hemconv_shared” and “sphereconv_hemconv_shared”. This approach is a variant of the inclusion of “invariances” into the neural network in the terminology of von Rueden et al. (2020). The rationale behind this flipping approach is that many properties of the atmospheric circulation have flipped properties on one hemisphere compared to the hemisphere. For example, many variables – including temperature and geopotential – have significant pole-to-equator gradients which change sign between the hemispheres. Additionally, mid-latitude weather systems spin in opposite directions in the two hemispheres which manifests itself, amongst others, in the temperature and geopotential fields. Note that when sharing the weights, but not flipping the weights, one would end up with the base architecture again. For both hemconv and hemconv_shared (and sphereconv_hemconv and sphereconv_hemconv_shared, respectively), for

TABLE 2. Overview of network architectures

architecture	parameters
basenet	336,040
sphereconv	336,040
hemconv	671,816
hemconv_halfsize	336,040
hemconv_shared	336,040
sphereconv_hemconv	671,816
sphereconv_hemconv_shared	336,040
basenet_latlon	336,040

each convolution operation, the same convolution depth (=number of filters) is used. Therefore, the networks of hemconv and sphereconv_hemconv have twice the number of parameters compared to the other architectures.

4) ADDITIONAL EXPERIMENTS

In the addition to using all architectures described above, we made two additional experiments on the low resolution data. In the first experiment we added latitude and longitude grids as constant input features to the input data. Latitude was scaled to $[0,1]$, while the longitude θ (in radians) was, just as day of the year and hour of the day, presented as two variables

$$lon1 = \sin(\theta) \tag{13}$$

$$lon2 = \cos(\theta) \tag{14}$$

$$\tag{15}$$

This approach we call base_latlon. In the second experiment, called hemconv_halfsize, we use hemispheric convolution without filter sharing, but with half the number of parameters per hemisphere compared to the base architecture. With this, the network in total has the same number of parameters as the base-architecture and all other architectures except for hemconv_shared and sphereconv_hemconv_shared. An overview of network architectures and the number of neural network parameters is given in table 2.

5) NETWORK TRAINING

For the training, the data from WeatherBench is converted to the tensorflow-record format. Each network is trained 4 times with different random seeds to account for the randomness in the training. Each training realization is evaluated separately, and throughout the paper the average of the errors and skill scores is shown. The same architecture is used for both high and low resolution data. Only the input size is adjusted according to the resolution. Since the architecture is a pure convolution architecture, the number of parameters (weights) is independent of the input size, and thus both for high-resolution and low-resolution the same number of parameters is used (336,040 for architectures with same weights for both hemispheres, and 671,816 for the architectures with independent weights for each hemisphere). We train the networks first for 100 epochs, and then over an additional 50 epochs with early stopping (stopping after no increase in skill at 10% of the training data left out for validation). The latter step is done to prevent overfitting of the model.

d. Forecast evaluation

We use both Root Mean Square Error (RMSE) and Anomaly Correlation Coefficient (ACC), which are also the two evaluation measures used in WeatherBench.

RMSE is defined as

$$RMSE = \overline{(fc - truth)^2} \quad (16)$$

with the overbar representing latitude-weighted area and time mean, and ACC as

$$ACC = corr(fc - clim, truth - clim) \quad (17)$$

with the correlation computed with latitude weights and *clim* the time-mean over all forecasts. For further details on the calculations, we refer the readers to Rasp et al. (2020).

3. Results

a. Evaluation of the different forecast architectures

We start by looking at global average RMSE and ACC, shown in Figs. 2 and 3 and Table 3. The upper panels of the figures show absolute values, whereas the lower panels show the differences

relative to the base architecture. The base architecture has the lowest skill at all lead times and for all resolutions, skill metrics and variables considered here (we do not include here the two additional experiments described in Sect. 2c), except for lead times of 6–8 days for RMSE of the low-resolution 850 hPa temperature. Sphereconv improves over the base architecture for all cases. This holds for all lead-times, both resolutions and both for RMSE and ACC. In many cases, the improvement is however relatively small.

The hemconv architecture also improves systematically on the base architecture, with the exception of the above-mentioned lead times of 6–8 days for RMSE of the low-resolution 850 hPa temperature. Depending on the variable, resolution and lead time, it can also perform better than than the sphereconv architecture on the high-resolution data. Taking as reference RMSE at lead times of 3 or 5 days (Table 3), sphereconv systematically outperforms hemconv. Combining the two (sphereconv_hemconv), the forecast performance generally improves further over both sphereconv and hemconv taken individually. The hemispheric convolution architecture with shared (flipped) weights (hemconv_shared) generally outperforms the hemispheric convolution architecture with independent weights. The same holds when comparing Spherenet convolution combined with hemisphere-wise convolution with shared weights (sphereconv_hemconv_shared) to sphereconv_hemconv. While no single method is the best for all cases considered, in most cases combining Spherenet convolution with hemisphere-wise convolution and sharing the flipped weights leads to the best results. This is illustrated in Table 3, where the lowest RMSE for each variable, lead time and resolution (not considering IFS) is highlighted in bold.

We now turn to the spatial distribution of RMSE. We focus on z500 as this provides a more direct link to the atmospheric circulation than temperature (Fig. 4). Panel a) shows the error of the base networks at different lead times for the high-resolution data, with increasing leadtime from upper left to lower right. The error pattern follows the typical error patterns of medium range NWP forecasts, with lowest predictability in the storm-track regions and in the Southern Hemisphere (e.g. Scher and Messori (2019a)). As expected, the error grows with increasing lead-time, with no dramatic changes in the spatial patterns.

More interesting is the difference between the spherconv and the base architecture (Fig. 4b) and between hemconv_sharedweights and the base architecture (Fig. 4c). Both clearly improve the forecasts in the high latitudes, and in particular in the Southern Hemisphere, with increasing

improvement with increasing lead times. We finally consider the difference between `sphereconv_hemconv_shared` and `hemconv_shared` (Fig. 4d). Up to forecast day 5, the Spherenet convolution clearly improves the forecasts around both poles. For longer lead times, the Spherenet convolution still provides an improvement, but this now appears to be largest in the mid-latitudes. Results are similar for t850 (Fig. A1), except that the forecast improvements in the mid-latitudes for both `sphereconv` and `hemconv_shared` are larger relative to those in the poles than for z500. Moreover, `sphereconv_hemconv_shared` presents a slightly lower skill in some mid-latitude regions compared to `hemconv_shared`.

Finally, we turn to the two additional experiments carried out on the low resolution data: including latitude and longitude as additional constant channels (`base_latlon`), and hemispheric convolution without shared weights, but with half the number of weights per convolution (`hemconv_halfsize`), thus in total the same number of weights as the base architecture. Adding longitude and latitude information, surprisingly, deteriorates forecast performance for z500, while it slightly increases forecast skill of t850 at intermediate lead times (second-to-last bars in Fig. 3). We however note that we have not tuned our model for these additional inputs, and we cannot exclude that the number of parameters and therefore the capacity of the network is not large enough to exploit this additional information. The results with the hemispheric convolution with same number of weights as the base architecture are also intriguing (last bars in Fig. 3). The forecast skill deteriorates compared to the base architecture, except for ACC at longer lead times, while for RMSE it deteriorates at all lead times. This result shows that the skill increase brought by the non-shared hemispheric convolution reported above actually seems to come from the higher number of parameters, and not from the separate convolutions. Conversely, the improved skill seen in the architecture with shared but flipped parameters clearly shows that the flipping provides an advantage.

b. Analysis of events with largest forecast errors

We now look at the forecasts within the upper 5% of RMSE (forecast “busts”) for the Northern Hemisphere (NH) for lead-time 3 days for the `sphereconv_hemconv_shared` architecture (the architecture which, as discussed in Sect. 3a, generally displays the highest forecast skill). For each of the 4 training realizations, the percentile is computed individually. When comparing the initialization dates of the worst forecasts, ~28% are exactly the same dates for all training realisations, ~46%

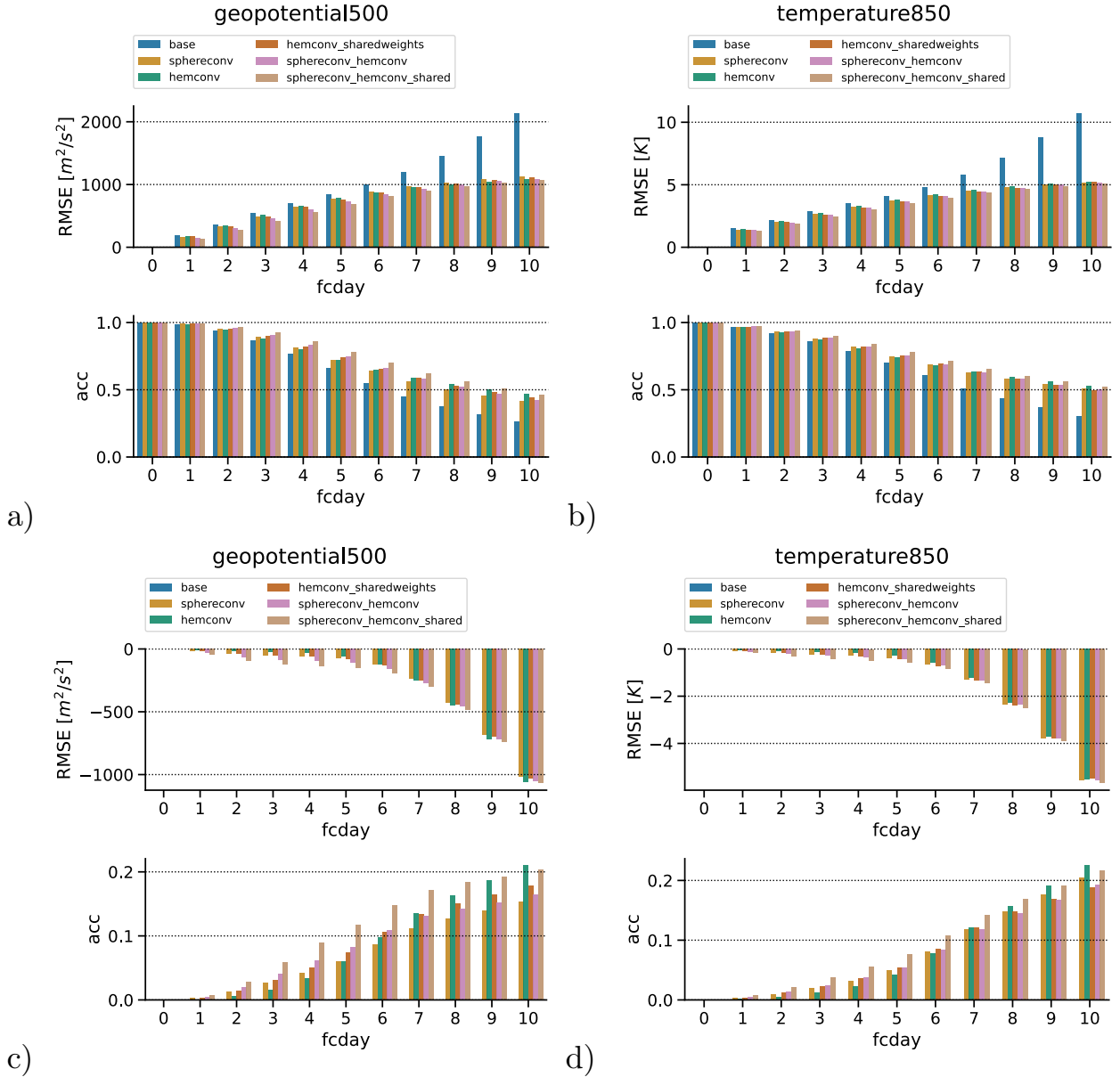


FIG. 2. Forecast skill (RMSE and ACC) for all high-resolution (1.4°) architectures for geopotential at 500hPa and temperature at 850hpa. a,b: absolute values; c,d: RMSE and ACC of all architectures minus RMSE and ACC of base architecture. For all plots: The ordering of the bars is the same as the ordering in the legend when read column-wise. The first column top to bottom corresponds to the first four bars, the second column to the remaining four bars.

occur in at least 3 of the 4 members, and $\sim 66\%$ in at least 2 of the 4 members (Fig. 5 a). This is much higher than expected by chance if the events were randomly distributed. Events with large errors are more common in boreal winter than in summer (Fig. 5 b), in line with the performance

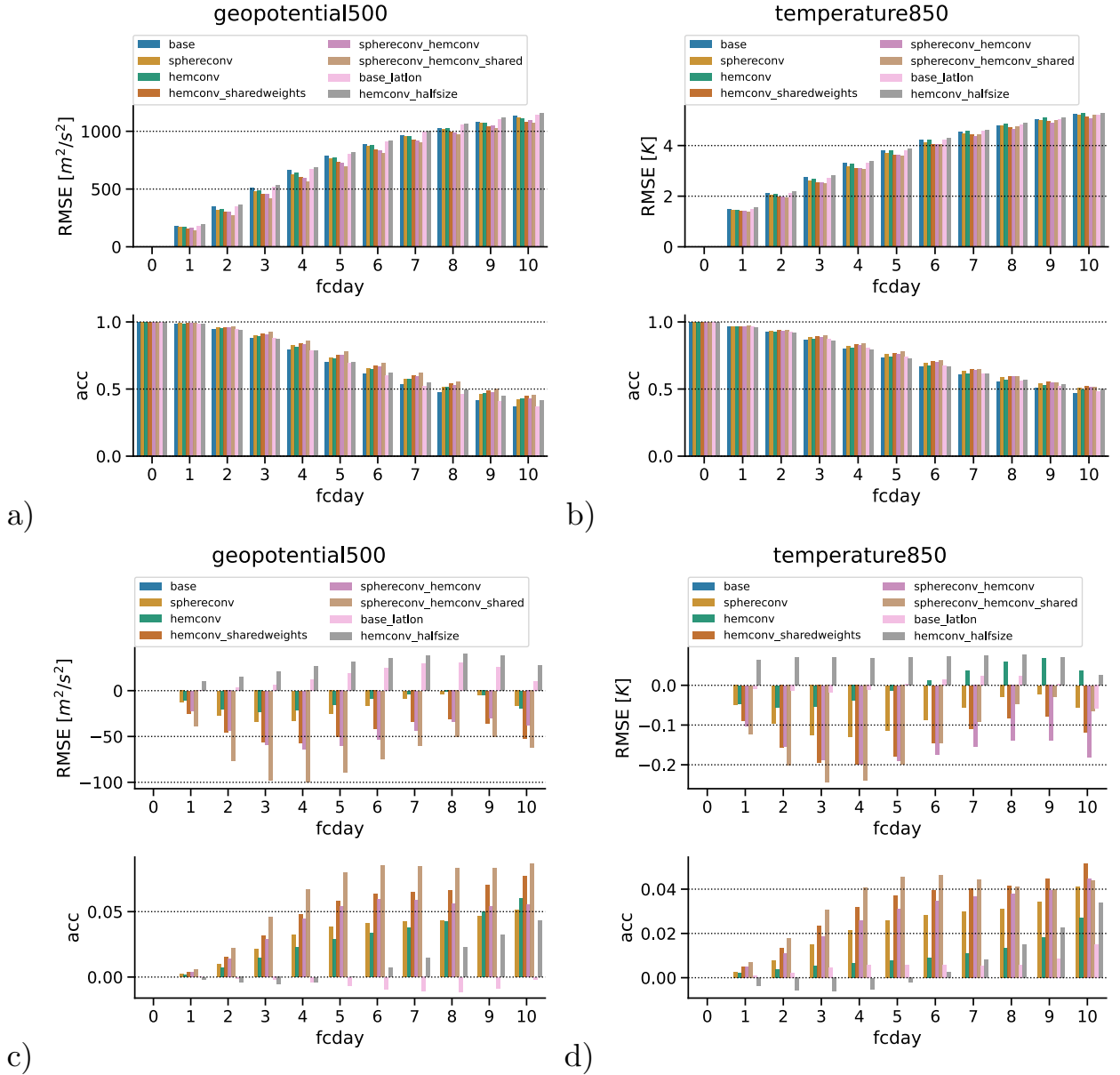


FIG. 3. Forecast skill (RMSE and ACC) for all low-resolution (2.8°) architectures, for geopotential at 500hPa and temperature at 850hpa. The figure includes the two additional experiments only performed on the low resolution data: namely providing latitude and longitude values as constant feature channels ("base_latlon") and hemispheric convolution with only half the number of parameters per hemisphere ("hemconv_halfsize") a,b: absolute values; c,d: RMSE and ACC of all architectures minus RMSE and ACC of base architecture. For all plots: The ordering of the bars is the same as the ordering in the legend when read column-wise. The first column top to bottom corresponds to the first four bars, the second column to the remaining four bars.

of operational NWP models. Similarly, repeating the analysis on Southern Hemisphere data shows that events with large errors are more common in austral winter (Fig. A2).

TABLE 3. RMSE at days 3 and 5, for all architectures, including NWP model scores as baselines. High-resolution is abbreviated as “hres”, low-resolution as “lres”. The numbers in parentheses denote the standard deviation of the errors between the 4 training realizations of each network. The lowest RMSE for each variable, lead time and resolution (not considering IFS) is highlighted in bold.

	geopotential 500hPa day 3 [m^2/s^2]	geopotential 500hPa day 5 [m^2/s^2]	temperature 850hPa day 3 [K]	temperature 850hPa day 5 [K]
hres base	542 (7)	845 (40)	2.87 (0.09)	4.11 (0.16)
hres hemconv	519 (15)	785 (24)	2.73 (0.07)	3.83 (0.11)
hres hemconv_sharedweights	492 (14)	767 (26)	2.61 (0.02)	3.68 (0.10)
hres sphereconv	487 (6)	773 (8)	2.64 (0.07)	3.73 (0.13)
hres sphereconv_hemconv	455 (13)	736 (28)	2.57 (0.02)	3.68 (0.04)
hres sphereconv_hemconv_shared	415 (6)	696 (11)	2.45 (0.05)	3.53 (0.08)
lres base	514 (14)	788 (26)	2.75 (0.08)	3.81 (0.12)
lres base_latlon	520 (17)	806 (34)	2.73 (0.03)	3.82 (0.07)
lres hemconv	490 (4)	773 (6)	2.69 (0.07)	3.80 (0.10)
lres hemconv_halfsize	535 (12)	819 (27)	2.82 (0.11)	3.88 (0.16)
lres hemconv_sharedweights	458 (18)	737 (33)	2.55 (0.05)	3.63 (0.07)
lres sphereconv	480 (13)	762 (20)	2.62 (0.08)	3.70 (0.14)
lres sphereconv_hemconv	455 (6)	727 (12)	2.56 (0.02)	3.62 (0.02)
lres sphereconv_hemconv_shared	416 (14)	699 (35)	2.50 (0.07)	3.61 (0.09)
IFS T42	489	743	3.09	3.83
IFS T63	268	463	1.85	2.52
Operational IFS	154	334	1.36	2.03

Finally, Fig. 5c) shows composite z500 anomalies at all initialisation times for which at least one of the spherconv_hemconv_shared high-resolution networks had an error > 95% in the NH. The anomaly is computed with respect to the mean over 2017–2018 (the evaluation period), and separately for each month. There are positive anomalies east of Greenland, in central Russia and in the middle of the North Pacific, and negative anomalies in northern Canada, the eastern coast of Asia and central Europe. There is also an anomaly dipole between the west coast of North America and the eastern Pacific, at lower latitudes than the other anomaly centres. These collectively constitute a circumhemispheric wave-4 pattern. The results are qualitatively similar for other architectures (Figs. A3–A5), and for other lead-times (Figs. A6–A9). This indicates that the skill of the network forecasts is dependent on the atmospheric configuration, just as in NWP forecasts (e.g. Ferranti et al. (2015); Matsueda and Palmer (2018)).

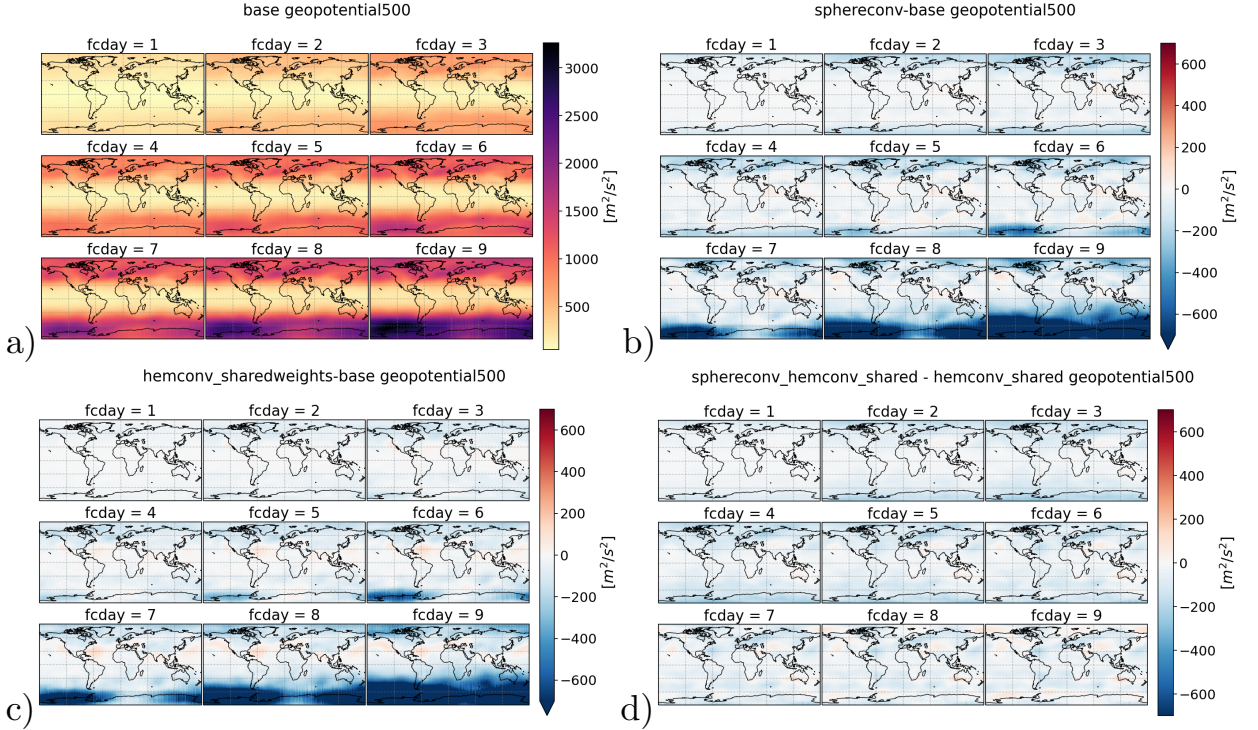
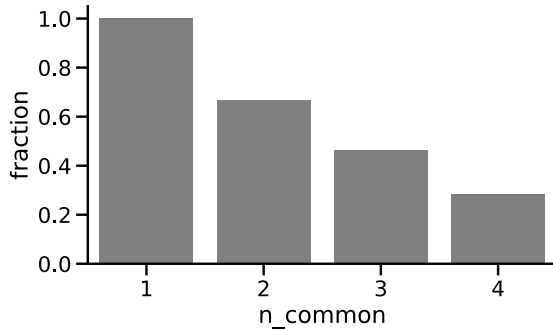


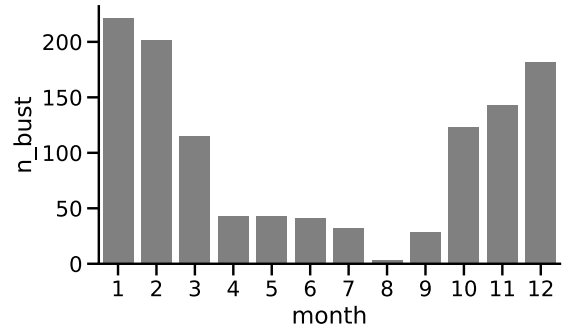
FIG. 4. a) Spatial distribution of RMSE of geopotential at 500 hpa [m^2/s^2] for forecasts days 1-9 of the base architecture; b) difference between RMSE of sphereconv and RMSE base; c) difference between RMSE of hemconv_shared and RMSE of base; and d) difference between RMSE of sphereconv_hemconv_shared and RMSE of hemconv_shared

c. Computational Performance

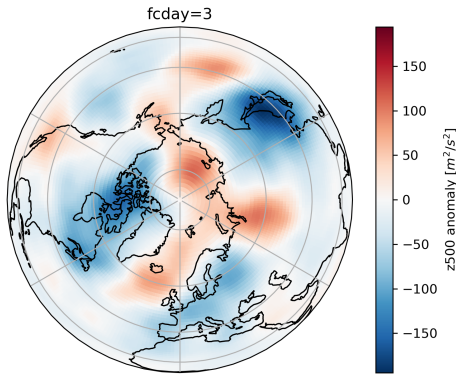
Replacing standard convolution with Spherenet convolution introduces a significant amount of additional computations. While the use of sparse tensorflow tensors (see Sect. 2.b) for the interpolation tensor \hat{L} avoids large memory requirements, the computation time of the sphereconv network for the high-resolution data compared to the base architecture is roughly a factor 8 higher on a CPU with 2 cores (9.3 vs 1.1s), and by a factor of 150 higher on a NVIDIA Tesla v100 GPU (3.3s vs 23ms). The computational overhead might be reduced by optimizing the implementation for certain computational architectures, such as in Esteves et al. (2023), who optimized their code for Tensor Processing Units (TPUs). Using hemisphere-wise convolution, on the other hand, does not introduce any significant performance overhead (with shared weights $\sim 4\%$, with separate weights none at all).



a)



b)



c)

FIG. 5. a) Fraction of dates with extreme forecast error (RMSE > 95%) in the Northern Hemisphere (NH) that occur in at least n_{common} out of the 4 training realisation for `sphereconv_hemconv_shared`. b) Monthly count of days with at least one training realisation with extreme forecast error in the NH. c) Composite anomalies of z_{500} on all initialisation dates for which at least one training realisation has an extreme forecast error at leadtime 3 days in the NH. The anomalies are computed relative to deseasonalized (monthly) means. All data is from the high resolution forecasts over the period 2017–2018.

4. Discussion and Conclusion

In this paper, we have tested two approaches to improve data-driven weather forecasts with CNNs. The aim was not to develop the best possible neural network based weather forecasts (and indeed we note that there are publications presenting data-driven forecasts with a higher skill than ours), but to assess the effect of specific changes to a conventional neural network architecture on forecast skill. Firstly, we have tested replacing standard convolution operations with a convolution operation that takes into account the (near-)spherical shape of the Earth. Secondly, we tested integrating basic meteorological knowledge into the structure of the networks, namely that the dynamics of the two hemispheres are different. This is done in two ways: in the first case, we

hardcode into the network that the dynamics of one hemisphere are “flipped” with respect to the other hemisphere. This is implemented by flipping the weights of the network. In the second case, we use independent weights for each hemisphere, thus leaving the network free to learn potential differences in dynamics. These methods (and combinations of them) were tested on the ERA5 data from the WeatherBench dataset (Rasp et al. 2020). We used a neural network architecture previously proposed by Weyn et al. (2020), and adapted it to our convolution methods. We found that both the Spherenet convolution and the hemispheric information improve the forecasts, but in subtly different ways. Both Spherenet convolution and flipped hemispheric information lead to the largest improvements close to the poles, and less so in other regions. However, adding the Spherenet convolution to the flipped hemisphere-specific information leads to relatively uniform improvements in the mid-latitudes when compared to hemispheric information alone. The mid-latitudes are the regions where the largest forecast errors appear in the first place. For most lead times, skill metrics, resolutions and variables considered here, combining Spherenet convolution with hemisphere-specific information using shared flipped weights leads to the best forecasts. The experiments with hemispheric convolution without weight sharing show some interesting results. While hemispheric convolution without weight sharing showed a skill increase, the additional experiment with keeping the number of parameters the same as in the base architecture showed that this skill increase actually seems to come mainly from the additional parameters, and not the hemispheric convolution. This however clearly shows that the skill increase in the hemispheric convolution *with* shared convolution comes from the weight-sharing and flipping, showing the value of this physics-inspired approach.

Finally, we have found that initial conditions causing the largest forecast errors are relatively consistent across different training realizations of the same network, and across different network architectures and lead times. This indicates that, as for conventional NWP forecasts, forecast errors of the neural networks are at least partly flow-dependent. In other words, the networks struggle to make skilful forecasts when initialised from specific atmospheric states. Previous work has shown that quantifications of an “intrinsic” atmospheric predictability only partly match the empirical forecast errors from a NWP initialised from that atmospheric state (Scher and Messori 2018; Hochman et al. 2019, 2021, 2022). We do not investigate here whether the atmospheric configurations leading to high forecast errors for the CNNs used here match configurations with

low ‘intrinsic’ atmospheric predictability. Indeed, the error could also depend on the error in the reanalysis product used for training or on deficiencies in the training of the networks themselves.

Possible improvements to the methods presented here could be:

- To split up the convolution for smaller regions instead of at hemispheric scale (similar to Weyn et al. (2020)), which could lead to the shared flipped weights no longer presenting a forecast skill advantage over independent convolutions.
- To include locally connected layers. Here each gridpoint in a layer is also a combination of the inputs from a certain kernel (e.g. 3×3), but the weights are not shared across the domain.
- To add more prior information into the structure of the network, for example on the vertical structure of the atmosphere.

In this study, we used an existing architecture, and changed the convolution types. Due to limited computational resources, we did not perform any additional hyperparameter tuning. An additional methodological improvement would therefore be to tune each individual architecture separately. Related to this, one could also compare scores for the training set both between architectures and to those on the test set, to verify whether any over or under fitting is occurring for the different models.

Our approach differs from previous studies in the field in several respects. The closest previous work is that by Weyn et al. (2020), who split up the world into six regions — two polar and four equatorial regions — with each region being represented by a local grid. On these local grids they used standard convolution operations. This method still leads to distortions, as even a subregion of the Earth’s surface cannot be represented on a local regular grid with complete accuracy. In addition, this method also needs padding at the edge of each of the 6 regions, which introduces some ambiguity at the corners. Weyn et al. (2020) further use two sets of weights, one for all four equatorial regions and the other one for the two polar regions. The weights for the polar regions are “flipped” between the two poles. This is similar to our idea of flipped weights to provide hemispheric information to the CNN. There are also several differences between the approach we present here and that of Weyn et al. (2020) from a practical point of view. The method of Weyn et al. (2020) needs data-preprocessing (regridding), but can then use standard neural

network operations. In our approach, the standard data can be used, but the Spherenet convolution introduces a computational overhead in every pass through the network.

The percent increase in runtime needed for the networks with Spherenet convolution is higher on a GPU than on CPU, which could indicate that the implementation using sparse tensorflow tensors – which we adopt here – is not optimized for GPUs. For small input sizes, an alternative would be to use standard tensorflow tensors (still filled sparsely, but represented as a full tensor (array) in memory). However, for the full resolution ERA5 data (0.25° resolution, namely 3600×1801 gridpoints on a regular lat-lon points), this would not be feasible with current computers due to memory limitations. Indeed, the interpolation tensor would then have a size of 6483600×6483600 .

The methods used and presented in this study all generate single deterministic forecasts. In many weather forecasting settings, however, probabilistic forecasts are wanted. The typical way to do this with numerical weather prediction models is to use ensemble forecasting, which entails performing multiple model runs with slightly different initial conditions, slightly different model formulations, stochastic components, or a combination of these (e.g. (Leutbecher and Palmer 2008)). While dedicated probabilistic ML techniques exist, such as gaussian process regression (Ebden 2015) or probabilistic neural networks (Mohebbi et al. 2020), the at least conceptually simpler approach is to apply the concept of ensemble NWP to ML models as well. Scher and Messori (2020) compared three methods of generating ensembles from deterministic neural network prediction systems. The first one – using multiple models, each trained with different initial seeds, has a computational cost which scales linearly with ensemble size both in the training stage and the prediction stages. Using random initial perturbations requires no additional training, and scales linearly in the prediction phase with no significant additional overhead, as generating the random perturbations is computationally cheap. The final and most advanced method uses singular value decomposition to find optimal initial perturbations. This introduces a one-time overhead per prediction for generating the singular vectors for the initial perturbations, and apart from this the computational cost again scales linearly with ensemble size. In principle, the improvements to conventional CNNs proposed here would be combined with any of the above approaches, although the one requiring to train the model multiple times may become computationally demanding given the additional overhead from the Spherenet convolution.

To conclude, in this study we have tested some simple improvements to conventional convolutional neural network architectures for weather forecasting. These are based on a convolution operator accounting for the Earth’s (near-)spherical geometry and on providing the network with knowledge that the climate dynamics of the two hemispheres differ. We did not seek to outperform state-of-the-art data-driven weather forecasts in terms of forecast skill but instead sought to test the limits of CNNs with a relatively small number of parameters. This can be beneficial for research groups who may not have enough computational capacity to run very large transformer or GNN models. The improvements presented here stem from physical reasoning, and may support future development of physics-oriented ML weather prediction models.

Acknowledgments. S.S. was funded by the Dept. of Meteorology of Stockholm University. G.M. was supported by the European Union’s H2020 research and innovation programme under ERC grant no. 948309 (CENÆproject) and by the Swedish Research Council Vetenskapsrådet (grant no.: 2016–03724). This work was partly supported by the “DDAI” COMET Module within the COMET – Competence Centers for Excellent Technologies Programme, funded by the Austrian Federal Ministry (BMK and BMDW), the Austrian Research Promotion Agency (FFG), the province of Styria (SFG) and partners from industry and academia. The COMET Programme is managed by FFG. The computations and data handling were enabled by resources provided by the National Academic Infrastructure for Supercomputing in Sweden (NAISS) and the Swedish National Infrastructure for Computing (SNIC) at the High Performance Computing Center North (HPC2N) and National Supercomputer Centre (NSC), partially funded by the Swedish Research Council through grant agreements no. 2022-06725 and no. 2018-05973.

Data availability statement. The software developed for this study and the intermediate data underlying the plots are available on the first Authors github repository <https://github.com/sipposip/physics-informed-ML-NWP> as well as on zenodo <https://zenodo.org/record/8344872> with doi [10.5281/zenodo.8344872](https://doi.org/10.5281/zenodo.8344872). Additionally, the trained models are available stored in the zenodo archive as well. The ERA5 WeatherBench data used as input data can be freely obtained via WeatherBench <https://github.com/pangeo-data/WeatherBench> and alternatively as raw data freely from the Copernicus data store at <https://cds.climate.copernicus.eu/cdsapp#!/dataset/reanalysis-era5-single-levels?tab=overview>

APPENDIX

Additional analyses

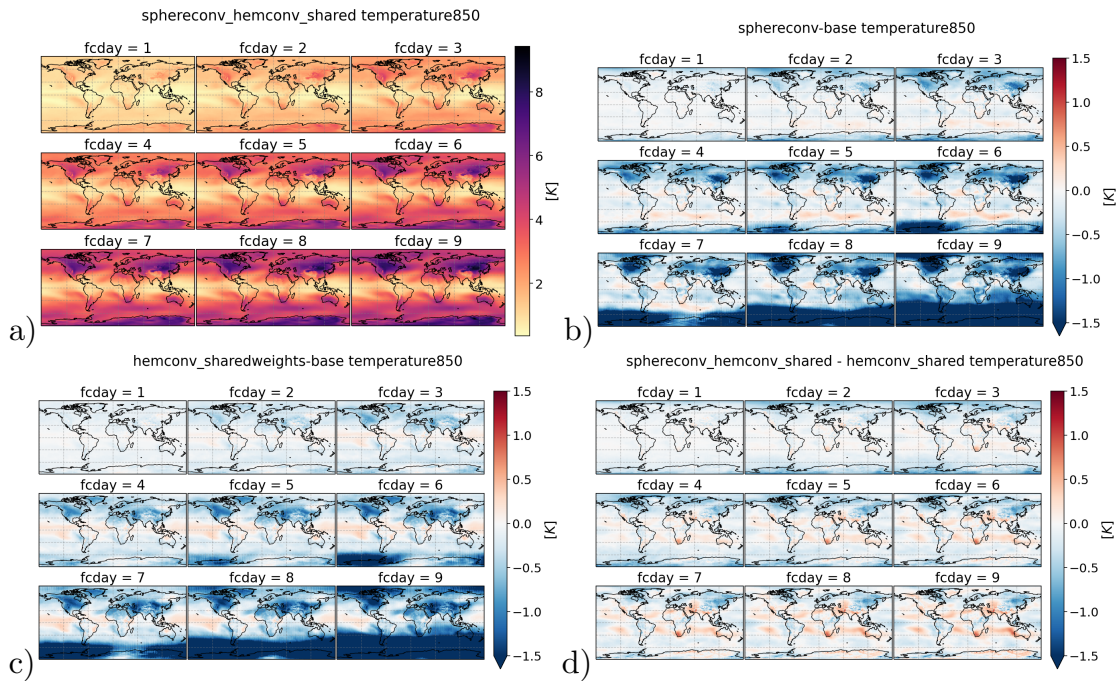


FIG. A1. As Fig. 4, but for t_{850} [K]

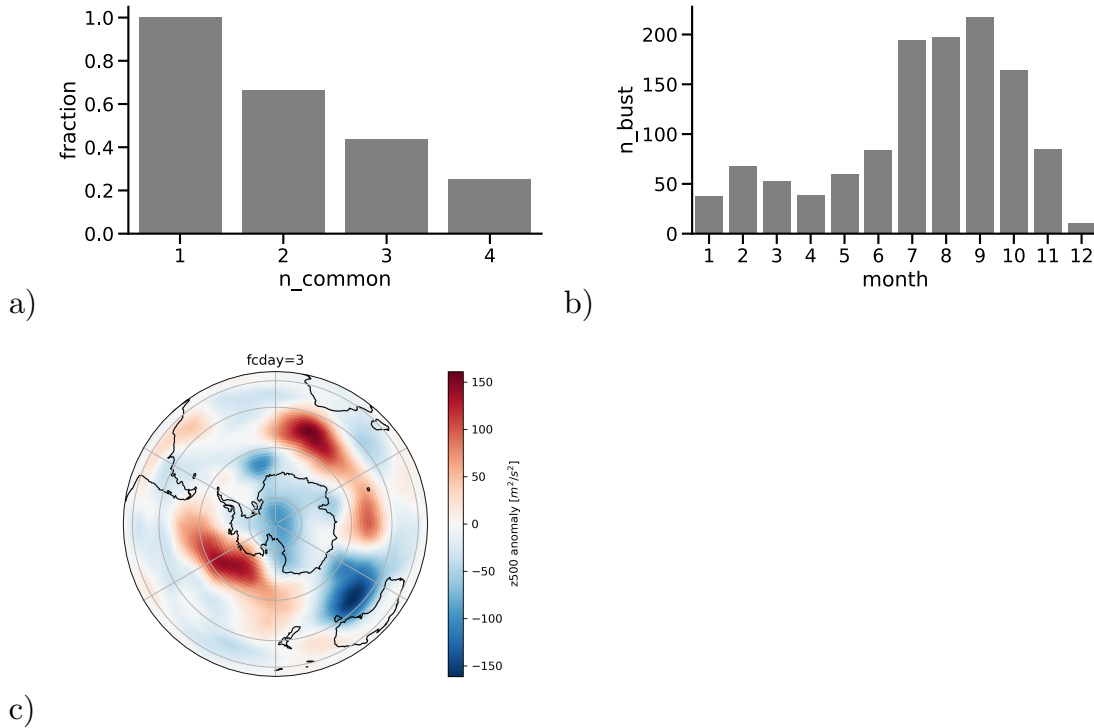
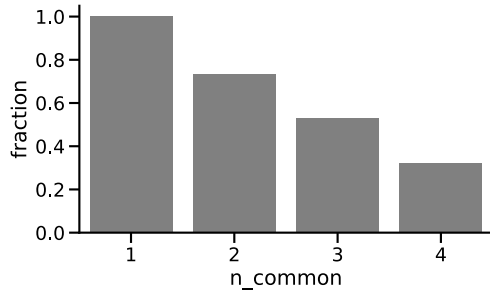
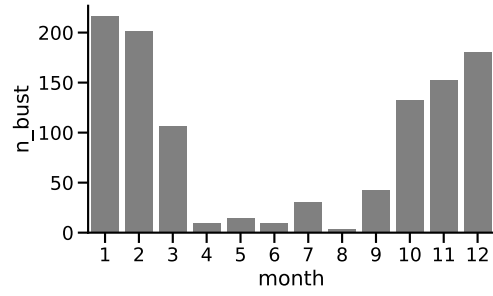


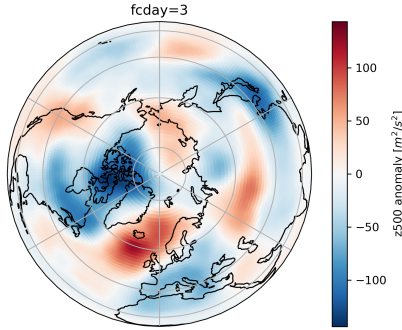
FIG. A2. As Fig. 5, but for the Southern Hemisphere



a)

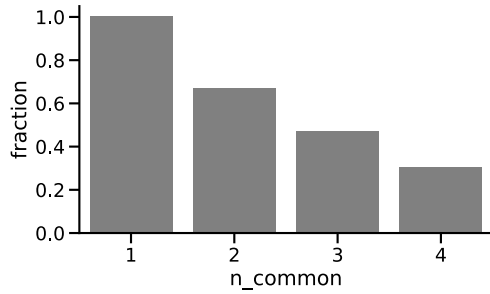


b)

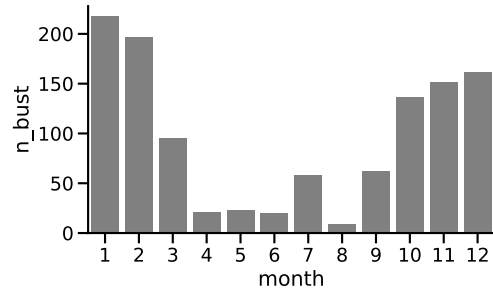


c)

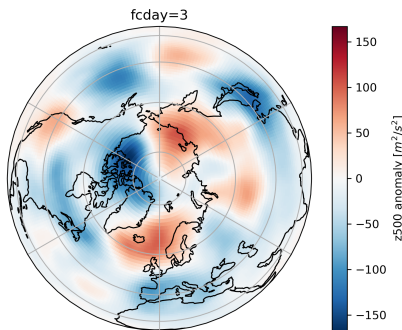
FIG. A3. As Fig. 5, but for the base architecture.



a)

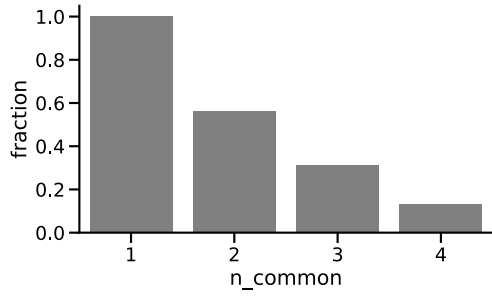


b)

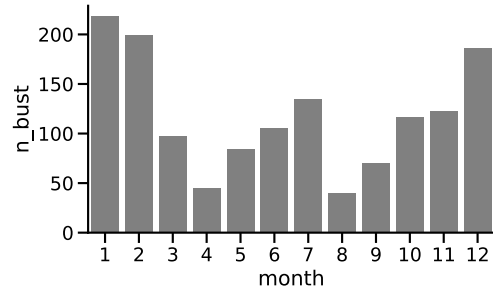


c)

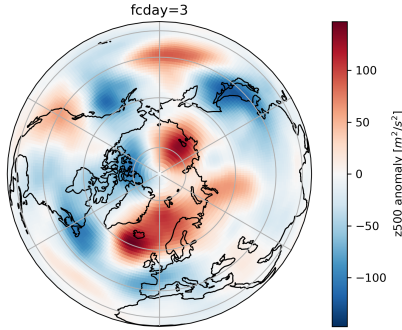
FIG. A4. As Fig. 5, but for the hemconv_shared architecture.



a)

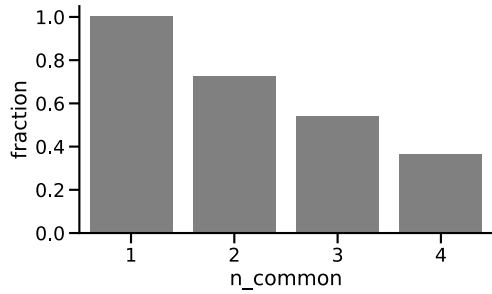


b)

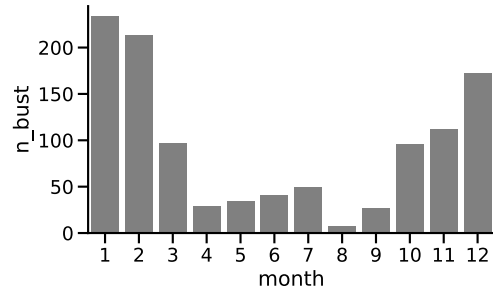


c)

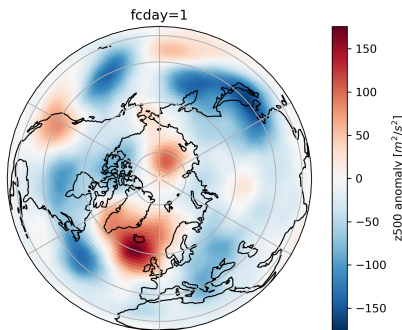
FIG. A5. As Fig. 5, but for the sphereconv architecture.



a)

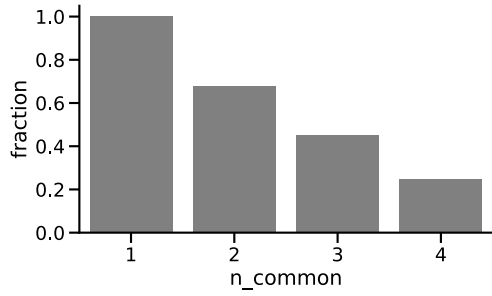


b)

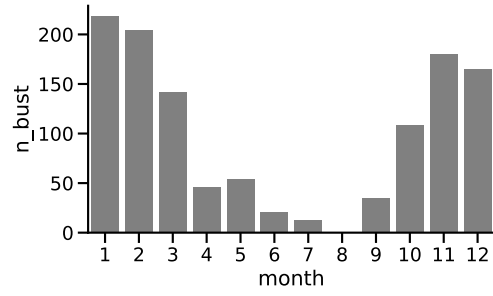


c)

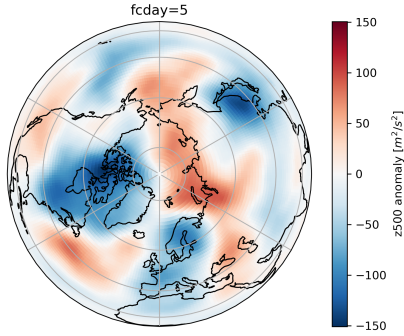
FIG. A6. As Fig. 5, but for lead time of 1 day.



a)

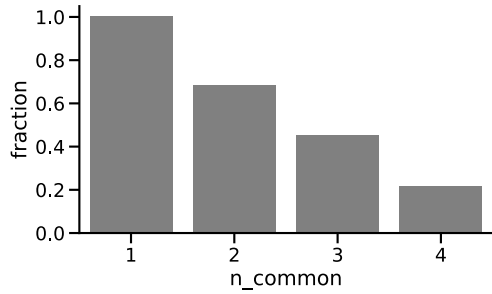


b)

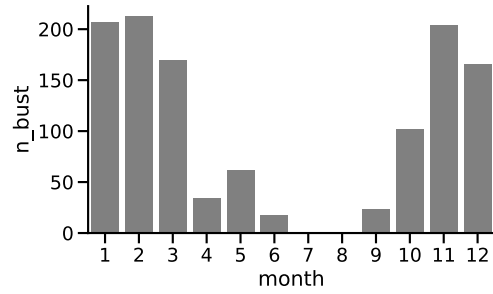


c)

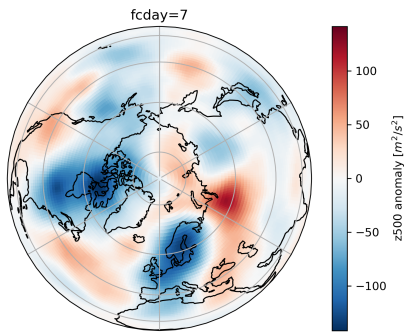
FIG. A7. As Fig. 5, but for lead time of 5 days.



a)

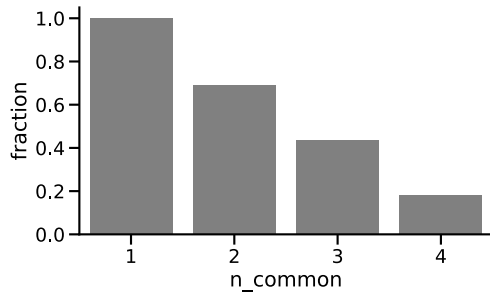


b)

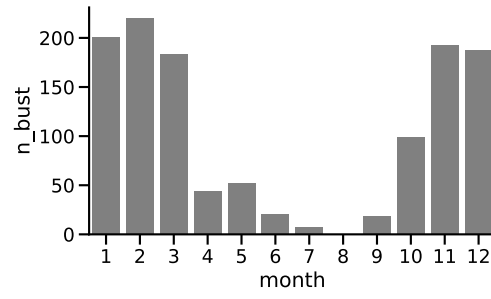


c)

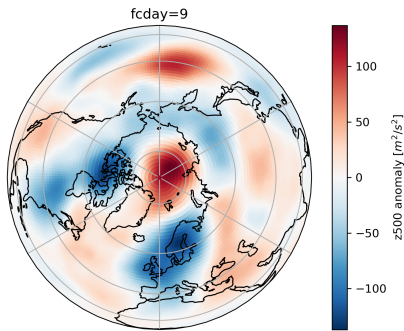
FIG. A8. As Fig. 5, but for lead time of 7 days.



a)



b)



c)

FIG. A9. As Fig. 5, but for lead time of 9 days.

References

- Arcomano, T., I. Szunyogh, A. Wikner, J. Pathak, B. R. Hunt, and E. Ott, 2022: A hybrid approach to atmospheric modeling that combines machine learning with a physics-based numerical model. *Journal of Advances in Modeling Earth Systems*, **14** (3), e2021MS002712.
- Balaji, V., 2020: Climbing down Charney's ladder: Machine Learning and the post-Dennard era of computational climate science. *arXiv:2005.11862 [nlin, physics:physics]*, 2005.11862.
- Bauer, P., A. Thorpe, and G. Brunet, 2015: The quiet revolution of numerical weather prediction. *Nature*, **525** (7567), 47–55, <https://doi.org/10.1038/nature14956>.
- Ben-Bouallegue, Z., and Coauthors, 2023: The rise of data-driven weather forecasting. 2307.10128.
- Bi, K., L. Xie, H. Zhang, X. Chen, X. Gu, and Q. Tian, 2022: Pangu-weather: A 3d high-resolution model for fast and accurate global weather forecast. 2211.02556.
- Boomsma, W., and J. Frellsen, 2017: Spherical convolutions and their application in molecular modelling. *Advances in neural information processing systems*, **30**.
- Chen, K., and Coauthors, 2023: Fengwu: Pushing the skillful global medium-range weather forecast beyond 10 days lead. 2304.02948.
- Cohen, T. S., M. Geiger, J. Köhler, and M. Welling, 2018: Spherical cnns. *CoRR*, **abs/1801.10130**, URL <http://arxiv.org/abs/1801.10130>, 1801.10130.
- Coors, B., A. P. Condurache, and A. Geiger, 2018: SphereNet: Learning Spherical Representations for Detection and Classification in Omnidirectional Images. *Computer Vision – ECCV 2018*, V. Ferrari, M. Hebert, C. Sminchisescu, and Y. Weiss, Eds., Springer International Publishing, Cham, 525–541, Lecture Notes in Computer Science.
- Dueben, P. D., and P. Bauer, 2018: Challenges and design choices for global weather and climate models based on machine learning. *Geoscientific Model Development*, **11** (10), 3999–4009, <https://doi.org/10.5194/gmd-11-3999-2018>.
- Ebden, M., 2015: Gaussian processes: A quick introduction. *arXiv preprint arXiv:1505.02965*.
- Eder, M., T. Price, T. Vu, A. Bapat, and J.-M. Frahm, 2019: Mapped convolutions. 1906.11096.

- Esteves, C., J.-J. Slotine, and A. Makadia, 2023: Scaling spherical cnns. 2306.05420.
- Faranda, D., and Coauthors, 2021: Enhancing geophysical flow machine learning performance via scale separation. *Nonlinear Processes in Geophysics*, **28** (3), 423–443.
- Ferranti, L., S. Corti, and M. Janousek, 2015: Flow-dependent verification of the ECMWF ensemble over the Euro-Atlantic sector. *Quarterly Journal of the Royal Meteorological Society*, **141** (688), 916–924, <https://doi.org/10.1002/qj.2411>.
- Hochman, A., P. Alpert, T. Harpaz, H. Saaroni, and G. Messori, 2019: A new dynamical systems perspective on atmospheric predictability: Eastern mediterranean weather regimes as a case study. *Science advances*, **5** (6), eaau0936.
- Hochman, A., S. Scher, J. Quinting, J. G. Pinto, and G. Messori, 2021: A new view of heat wave dynamics and predictability over the eastern mediterranean. *Earth System Dynamics*, **12** (1), 133–149.
- Hochman, A., S. Scher, J. Quinting, J. G. Pinto, and G. Messori, 2022: Dynamics and predictability of cold spells over the eastern mediterranean. *Climate Dynamics*, **58** (7-8), 2047–2064.
- Jiang, C. M., J. Huang, K. Kashinath, Prabhat, P. Marcus, and M. Nießner, 2019: Spherical cnns on unstructured grids. *CoRR*, **abs/1901.02039**, URL <http://arxiv.org/abs/1901.02039>, 1901.02039.
- Kashinath, K., and Coauthors, 2021: Physics-informed machine learning: case studies for weather and climate modelling. *Philosophical Transactions of the Royal Society A*, **379** (2194), 20200093.
- Keisler, R., 2022: Forecasting Global Weather with Graph Neural Networks. arXiv, URL <http://arxiv.org/abs/2202.07575>, arXiv:2202.07575 [physics], <https://doi.org/10.48550/arXiv.2202.07575>.
- Lam, R., and Coauthors, 2023: Graphcast: Learning skillful medium-range global weather forecasting. 2212.12794.
- Leutbecher, M., and T. N. Palmer, 2008: Ensemble forecasting. *Journal of computational physics*, **227** (7), 3515–3539.

- Lillo, S. P., and D. B. Parsons, 2017: Investigating the dynamics of error growth in ECMWF medium-range forecast busts. *Quarterly Journal of the Royal Meteorological Society*, **143 (704)**, 1211–1226, <https://doi.org/10.1002/qj.2938>.
- Martín Abadi, and Coauthors, 2015: *TensorFlow: Large-Scale Machine Learning on Heterogeneous Systems*.
- Matsueda, M., and T. Palmer, 2018: Estimates of flow-dependent predictability of wintertime euro-atlantic weather regimes in medium-range forecasts. *Quarterly Journal of the Royal Meteorological Society*, **144 (713)**, 1012–1027.
- Mohebbi, B., A. Tahmassebi, A. Meyer-Baese, and A. H. Gandomi, 2020: Chapter 14 - probabilistic neural networks: a brief overview of theory, implementation, and application. *Handbook of Probabilistic Models*, P. Samui, D. Tien Bui, S. Chakraborty, and R. C. Deo, Eds., Butterworth-Heinemann, 347–367, <https://doi.org/https://doi.org/10.1016/B978-0-12-816514-0.00014-X>, URL <https://www.sciencedirect.com/science/article/pii/B978012816514000014X>.
- Pathak, J., and Coauthors, 2022: FourCastNet: A Global Data-driven High-resolution Weather Model using Adaptive Fourier Neural Operators. arXiv, URL <http://arxiv.org/abs/2202.11214>, arXiv:2202.11214 [physics], <https://doi.org/10.48550/arXiv.2202.11214>.
- Rasp, S., P. D. Dueben, S. Scher, J. A. Weyn, S. Mouatadid, and N. Thuerey, 2020: WeatherBench: A benchmark dataset for data-driven weather forecasting. *arXiv:2002.00469 [physics, stat]*, 2002.00469.
- Rasp, S., and N. Thuerey, 2021: Data-driven medium-range weather prediction with a resnet pretrained on climate simulations: A new model for weatherbench. *Journal of Advances in Modeling Earth Systems*, **13 (2)**, e2020MS002405.
- Rodwell, M. J., and Coauthors, 2013: Characteristics of Occasional Poor Medium-Range Weather Forecasts for Europe. *Bulletin of the American Meteorological Society*, **94 (9)**, 1393–1405, <https://doi.org/10.1175/BAMS-D-12-00099.1>.
- Scher, S., 2018: Toward Data-Driven Weather and Climate Forecasting: Approximating a Simple General Circulation Model With Deep Learning. *Geophysical Research Letters*, **0 (0)**, <https://doi.org/10.1029/2018GL080704>.

- Scher, S., and G. Messori, 2018: Predicting weather forecast uncertainty with machine learning. *Quarterly Journal of the Royal Meteorological Society*, **144** (717), 2830–2841, <https://doi.org/10.1002/qj.3410>.
- Scher, S., and G. Messori, 2019a: How Global Warming Changes the Difficulty of Synoptic Weather Forecasting. *Geophysical Research Letters*, **46** (5), 2931–2939, <https://doi.org/10.1029/2018GL081856>.
- Scher, S., and G. Messori, 2019b: Weather and climate forecasting with neural networks: Using GCMs with different complexity as study-ground. *Geoscientific Model Development Discussions*, 1–15, <https://doi.org/10.5194/gmd-2019-53>.
- Scher, S., and G. Messori, 2020: Ensemble neural network forecasts with singular value decomposition. *arXiv:2002.05398 [physics]*, 2002.05398.
- von Rueden, L., and Coauthors, 2020: Informed Machine Learning – A Taxonomy and Survey of Integrating Knowledge into Learning Systems. *arXiv:1903.12394 [cs, stat]*, 1903.12394.
- Weyn, J. A., D. R. Durran, and R. Caruana, 2019: Can Machines Learn to Predict Weather? Using Deep Learning to Predict Gridded 500-hPa Geopotential Height From Historical Weather Data. *Journal of Advances in Modeling Earth Systems*.
- Weyn, J. A., D. R. Durran, and R. Caruana, 2020: Improving data-driven global weather prediction using deep convolutional neural networks on a cubed sphere. *Earth and Space Science Open Archive*, <http://www.essoar.org/doi/10.1002/essoar.10502543.1>, <https://doi.org/10.1002/essoar.10502543.1>.